Detection of Land Surface Temperature anomalies using ECOSTRESS in Olkaria geothermal field

Agnieszka Soszynska [a,b,*], Thomas Groen [a], Eunice Bonyo [c], Harald van der Werff [a], Robert Hewson [d], Robert Reeves [e], Christoph Hecker [a]

[a] Department of Applied Earth Sciences, Faculty ITC, University of Twente, Hengelosestraat 99, PO Box 217, Enschede, 7500 AE, The Netherlands
[b] School of Physics and Astronomy, University of Leicester, National Centre for Earth Observation, 92 Corporation Road, Leicester, LE4 5SP, United Kingdom
[c] Kenya Electricity Generating Company PLC, Off Moi Southlake Road, P.O. Box 785, Naivasha, 20117, Kenya
[d] Independent researcher, PO Box 245 Trentham, Victoria, 3458, Australia
[e] GNS Science, 114 Karetoto Road, RD4, Taupō, 3384, New Zealand

ARTICLE INFO

ABSTRACT

Geothermal systems can be used to produce low-emission energy throughout the day and night, regardless of the weather conditions. These features make geothermal systems a sustainable and reliable energy source, which can be exploited on a much larger scale than it is now. Remote sensing techniques can support detecting areas potentially suitable for geothermal energy production, thereby reducing the costs of preliminary exploration. The Ecosystem Spaceborne Thermal Radiometer Experiment on Space Station (ECOSTRESS) can provide nighttime thermal imagery, which can be used for geothermal anomaly detection. This paper presents a method for automated detection of geothermal anomalies using nighttime ECOSTRESS data of the study area in Olkaria, Kenya. The proposed detection method is a kernel-based one, and includes adaptions of kernel size for the cases of large geothermal anomalies. The accuracy of the method is verified with reference data acquired during field work. A producer's accuracy of 82% is achieved, which is on average 56% points better than in randomised anomaly maps. The possible sources of errors in detection are heat capacity of surfaces, terrain features and vegetation masking the thermal signatures. The high producer's accuracy proves potential for application in global mapping of geothermal anomalies.

1. Introduction

In the current situation of climate change, a transition towards sustainable energy sources is urgently needed. One of the renewable energy sources with low CO_2 emissions is heat from volcanic geothermal systems, where fluids and steam contained in a subsurface reservoir are brought to the surface and steam is used to produce electricity (Dickson and Fanelli, 2013; DiPippo, 2012; Mock et al., 1997; van der Meer et al., 2014). As geothermal heat sources can be utilised constantly, they provide a reliable alternative to fossil fuel based electricity production (Lee, 2004). Geothermal resources could be used much more extensively than now, therefore it is important to find new geothermal energy sources on a global scale. For this purpose, remote sensing techniques can be used.

Presence of a geothermal system at depth is often accompanied by geothermal surface manifestations, such as hot water springs, steaming grounds, fumaroles and heated grounds (van der Meer et al., 2014;

Scott, 2012). Geothermal surface temperature spatial anomalies (further in text referred to as "geothermal anomalies") are areas, where heat from a geothermal system reaches the surface causing the surface temperature to rise enough to be detected as hotter than the surroundings. Sometimes, vegetation in such an area is scarce or phenology of vegetation differs from the surrounding vegetation; some soil discolouration, hydrothermal mineral deposits, or clay alteration may also be visible (van der Meer et al., 2014).

Geothermal systems can be detected in remote sensing imagery acquired from different sources: drone, aircraft, and satellite. Although using high-resolution imagery provided by drone and aircraft surveys allows resolving very fine details, such surveys are very costly and conducting them is dependent on multiple factors such as weather conditions (including wind), or permits to fly an aircraft or a drone, not to mention the high travel and customs expenses. Since using spaceborne imagery is independent of most of these obstacles (apart from cloud cover during acquisition) and is typically more cost-effective,

---

* Corresponding author at: School of Physics and Astronomy, University of Leicester, National Centre for Earth Observation, 92 Corporation Road, Leicester, LE4 5SP, United Kingdom.
E-mail address: agnieszka.soszynska@le.ac.uk (A. Soszynska).

therefore, this kind of data seem the most suitable for the primary exploration.

However, detection of geothermal anomalies in space-borne imagery is influenced by several factors, such as strength and size of the anomaly, its temperature, albedo, moisture content of the surface, steam interference, weather conditions at the acquisition time, viewing angle of the instrument, soil compaction, rock coherence, and land cover (Calvin et al., 2005; Coolbaugh et al., 2007; Qin et al., 2011; Vaughan et al., 2012; Watson et al., 2008). Additionally, a sensor needs specific features to detect an anomaly, such as high spatial resolution and detector sensitivity. Geothermal anomalies can be detected by identifying geothermal derived mineral deposits (Hewson et al., 2020; van der Meer et al., 2014), but the more direct method would be to detect surface thermal anomalies created by heat leakage to the surface. Such anomalies are often smaller than a typical pixel footprint of a space-borne thermal sensor (*e.g.*, 100 m in TIRS sensor of Landsat-8), and have a low temperature contrast to the surroundings, which poses a challenge for remote sensing based detection methods of geothermal anomalies (Vaughan et al., 2010, 2012; Gutiérrez et al., 2012).

Until now, there have been only few attempts for automated detection of geothermal anomalies using data of moderate spatial resolution (<100 m). Often, researchers visually compared thermal imagery (sometimes corrected for some of the aforementioned effects) to maps of known geothermally active areas and acknowledged visibility of anomalies, while not providing a method suited for automated detection (Abubakar et al., 2019; Chan and Chang, 2018; Chan et al., 2018; Prayogo et al., 2019; Yuhendra, 2020). Some researchers used thresholding techniques to automatically identify geothermal anomalies (Coolbaugh et al., 2007; Wang et al., 2019; Gemitzi et al., 2021), however the authors do not provide quantitatively assessed accuracy results, that provide an overall accuracy.

Global thresholding detection techniques, which are used to detect *e.g.*, forest fires, often cannot be used successfully, because geothermal anomalies are usually not the strongest source of thermal emission in an image (Wang et al., 2019; Coolbaugh et al., 2007). A similar situation is noted with coal fires (Hecker et al., 2007; Kuenzer et al., 2007; Zhang, 2004), which also produce only moderately anomalous (above background), sub-pixel sized temperature anomalies at the surface. In coal fire detection attempts, authors frequently propose using a kernel-based thresholding method to detect coal fires in, for example, Landsat-7 ETM+ and MODIS imagery (Kuenzer et al., 2007; Zhang, 2004). Such a method retrieves statistical outliers in image subsets, which can be suitable for geothermal anomaly detection as well.

Furthermore, selecting the optimal remote sensing dataset is paramount for the analysis, because its parameters can strongly influence the accuracy of detection. An ideal dataset for detecting geothermal anomalies would have bands in thermal infrared, high spatial resolution, revisit time of less than 10 days, and acquisition at pre-dawn local time. However, these parameters are challenging to fulfil: Only a few currently available thermal sensors have GSD <100 m, due to longer wavelength, with its implication on detector size and optical system. Moreover, the sensors with fine GSD typically have low revisit time, which decreases a probability of acquiring cloud free imagery. The most currently available sensors have Sun-synchronous orbits that have acquisition time in the early night, although imagery acquired pre-dawn is optimal for geothermal anomaly detection. Pre-dawn imagery is optimal for geothermal anomaly detection, because at this time the land masses have had the maximum time to radiate the accumulated solar heat, thereby increasing the contrast between a geothermal anomaly which stays hot overnight and its surroundings which cool down (Romaguera et al., 2018; Coolbaugh et al., 2007).

Researchers attempting to automatically detect geothermal anomalies mainly used imagery from ASTER and various sensors of the Landsat platform series e.g., Coolbaugh et al. (2007) and Watson et al. (2008). ASTER images seem to be suitable for detecting surface temperature anomalies due to high spatial resolution of data (90 m

within a swath width of 60 km), and multiple spectral bands in thermal infrared (Coolbaugh et al., 2007; Eneva et al., 2006; Vaughan et al., 2010). The advantage of using Landsat data is the large area coverage (swath width is 185 km in TIRS and very similar for other sensors of Landsat platforms) (Watson et al., 2008) with a high spatial resolution of 100 m in thermal sensors of Landsat-9 and Landsat-8. Despite the favourable spatial dimensions of Landsat and ASTER imagery, their fixed orbits do not allow for acquisitions at optimal pre-dawn times.

The ECOsystem Spaceborne Thermal Radiometer Experiment on Space Station (ECOSTRESS) is a thermal infrared instrument, which fulfils most of the above-mentioned requirements. The swath width of ECOSTRESS at 384 km is even larger than the swath width of Landsat's sensors, while the pixel footprint of its products is 70 m, which is finer than that of ASTER and Landsat series. ECOSTRESS data have not been used for automated detection of geothermal anomalies so far (as of 2023). Some studies started analysing the feasibility of using ECOSTRESS data in geothermal exploration, including Silvestri et al. (2020b) who used ECOSTRESS data in a study that compared temperatures sensed with ASTER, Landsat-8, and ECOSTRESS from geothermally active areas in Parco delle Biancane, Italy. The purpose of the study was to evaluate the reliability of the retrieved Land Surface Temperature (LST) for future geophysical studies in geothermal field, and concludes that ECOSTRESS provides a valuable data source for such analyses. Silvestri et al. (2020a) also used ECOSTRESS data in comparison to aircraft and drone imagery. Thus, a multiscale validation of ECOSTRESS data was conducted that confirmed its calculated LST. However, these studies only provide some punctual comparisons of retrieved LST and not a detailed study on detection feasibility with quantified accuracy results.

In the presented research, a method for the automated detection of LST anomalies in a geothermally active area using ECOSTRESS data is described. Our study area, located in Olkaria (Kenya), is an example of a geothermally active area in the East African Rift. The used method detects local statistical outliers in subsets of the study area to avoid errors being introduced by a global temperature threshold. The detected anomalies are validated using ground observations from field work and auxiliary maps.

2. Materials and methods

2.1. Study area

Our study area is located in the Olkaria region of Kenya (Fig. 1), south of Lake Naivasha. The area, which covers almost 400 km^2, is typical of the East African Rift, with volcanic geology and a mix of savanna vegetation. The whole terrain has a high elevation at approximately 2000 m above sea level. Numerous volcanic craters can be found there (such as Longonot volcano, Suswa caldera, and the Eburru volcanic complex), as well as old lava flows, hot grounds, and fumaroles (Hewson et al., 2020; Clarke et al., 1989).

The lithology consists of six main rock groups: the basement formations from the Pleistocene, Pre-Mau volcanics, Mau tuffs, plateau trachytes, Olkaria basalt and upper Olkaria volcanic (Omenda, 1998). The plateau trachytes, which can be found in the subsurface, are the holding rocks for the geothermal reservoir in the Olkaria East field, while the basalt (which can have up to 500 m thickness) serve as a cap rock (Clarke et al., 1989). The geologic structures in the Greater Olkaria area consist of a ring structure, the Ol'Njorowa gorge, and several fault lines cutting through the area (Munyiri, 2016) (Fig. 1).

Fumaroles in Olkaria exhibit temperatures ranging between 312–371 K (40–99 °C; with boiling temperature at 93.4 °C at the height of 2000 m above sea level), and the circulation of hydrothermal fluids can cause soil alteration, resulting in discolouration. In the altered areas, the vegetation cover is often scarce or only the so-called geothermal grass is present (*Fimbristylis exilis*; a species of grass growing typically in geothermally active areas).
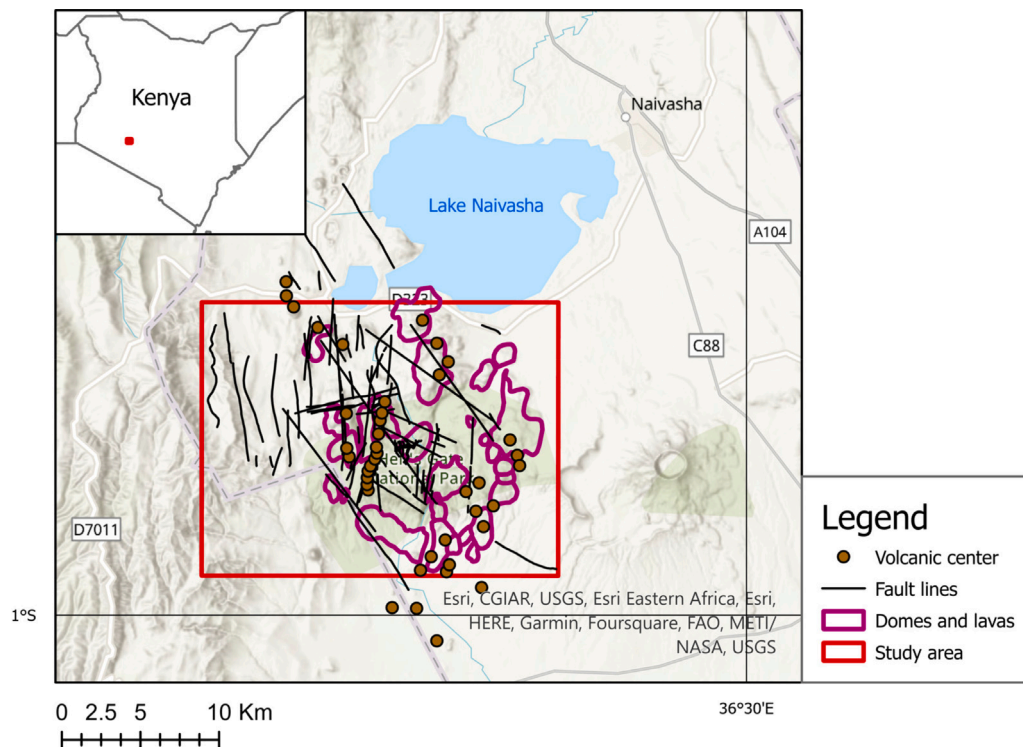
Fig. 1. The study area extent (red box) in Olkaria, Kenya. (For interpretation of the references to colour in this figure legend, the reader is referred to the web version of this article.)

Table 1
Specification of ECOSTRESS sensor and its LSTE product.

Parameter	Value
Wavelengths sensed [μm]	8.29, *8.78, 9.20, *10.49, 12.09
	*Not available for some datasets
Swath width	≈384 km
Nominal radiometric accuracy	0.5 K at 300 K
Revisit time	Irregular, ≈4 days
Acquisition time	Irregular, due to the precessing orbit of the ISS
Product name	Land Surface Temperature and Emissivity (LSTE)
Product pixel footprint	70 m

The geothermal exploration in Olkaria started in 1955, and commercial generation of electricity has been conducted since 1981. The geothermal power production is conducted in 5 large conventional single flash condensing type power plants and 16 well-head units with capacity of 799 MWe. Additionally, there are over 250 wells pumping hot brine-steam mixture to the power plants, or injecting cooled off water back into the reservoir.

2.2. Satellite data

The ECOSTRESS sensor is installed on the International Space Station (ISS), which has a precessing orbit, allowing acquisitions at different local times across day and night. ECOSTRESS was launched in mid-2018, and acquisition of images continues until September 2029 (Hook, 2023).[1] Due to its characteristics, such as high spatial resolution and large swath width (Table 1), ECOSTRESS can be important for geothermal anomaly detection.

In the processing, nighttime level-2 Land Surface Temperature and Emissivity (LSTE) ECOSTRESS products were used, which were acquired since the start of the mission. Images in which the majority of the study area was covered with clouds were excluded from the analysis; altogether, 22 mostly cloud-free all-nighttime images from Build 6 were used.[2] The list of the used datasets is provided in Table A.6.

The LSTE products are atmospherically corrected and have a spatial resolution of ≈70 × 70 m. L1B GEO products, containing geographic coordinates per pixel, were used for georeferencing. Further details on the image product used can be found in Hook and Hulley (2018). An example of ECOSTRESS images is presented in Fig. 2.

2.3. Auxiliary data

Several auxiliary datasets were used in the validation, which are described in detail below. The datasets are presented in Fig. 3, and comprise:

Soil temperature measurements from a field campaign. During a field campaign conducted in March 2022, 56 sites in the study area were visited to create a ground validation dataset. The locations of the ground validation sites were chosen based on a preliminary anomaly map, locations of fumaroles, hot grounds, and other features suggesting the existence of an LST anomaly. While visiting the locations during field work, a temperature measurement was made right beneath (≈1 mm depth) the soil surface and at 20 cm depth, resulting in two classes: geothermal and non-geothermal. The temperature measurements were conducted using Tempmate M1 sensors with extensions for the areas where the temperature was above 343 K. The accessibility of the terrain influenced the spatial distribution of the ground validation sites

---

[1] More information can be found in https://ecostress.jpl.nasa.gov/.

[2] Build 7.1 was released in November 2022, and backwards processing of the archive has started in January 2023 and is not finished as of 2023.
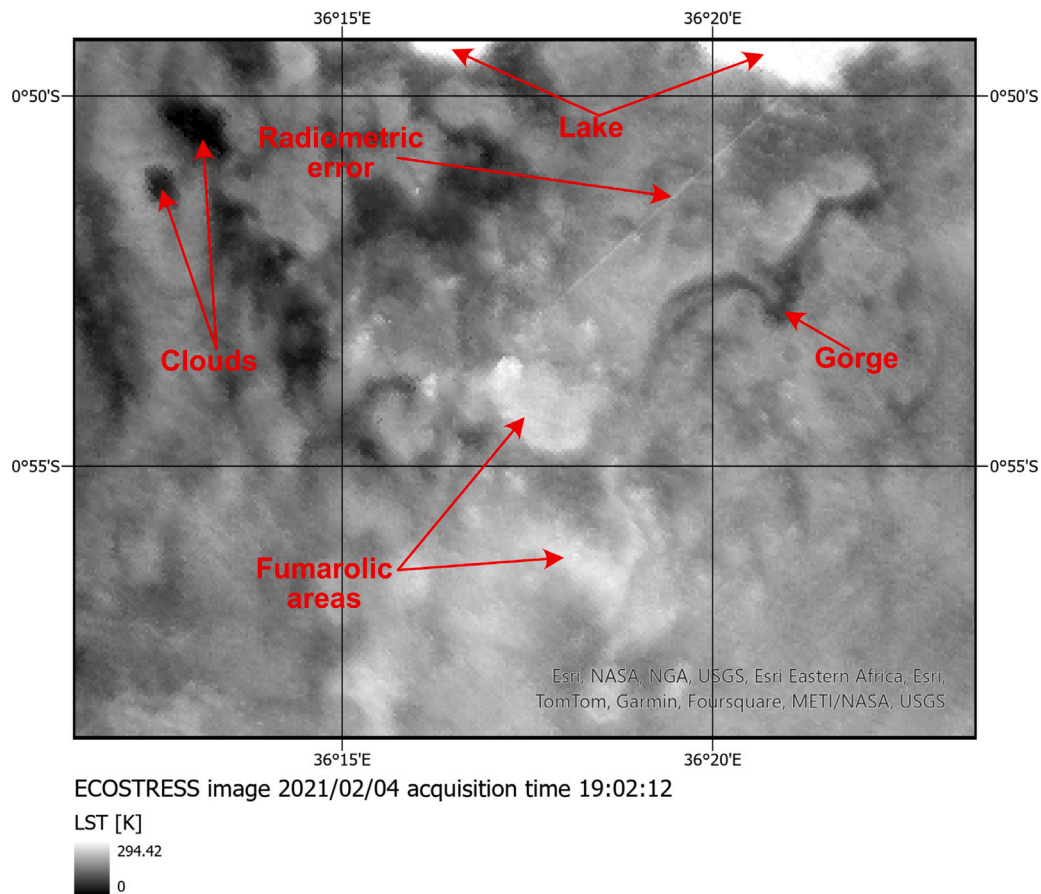
Fig. 2. Example ECOSTRESS LST product; image acquired on the 4th April 2021, at 19:02 UTC (22:02 local time). For illustrative purposes, an image before masking is presented, with annotations for ease of interpretation.

and caused that the size of the classes is not equal. We discuss the consequences of the class size inequality in Section 4.

In the ground validation data, the sampling locations, where temperatures at 20 cm depth surpassed the surface temperatures by more than 5 K, or the temperature at 20 cm depth exceeded 313 K, are considered geothermal areas. Contrary, non-geothermal areas are typically cooler at depth (but allowing up to 5 K above the surface temperatures, to account for sudden weather changes), and the temperature at 20 cm depth does not exceed 313 K.

Additionally, information regarding vegetation cover and type, the presence of hydrothermal alteration (such as discolouration of the soil), and any other signs of geothermal activity were noted at each location. Based on these pieces of information, the ground validation sites were divided into two categories, indicating presence or absence of geothermal anomalies.

Fumarole and heated ground location layer. Another validation dataset used, was a GIS layer containing locations of fumaroles and heated grounds. The layer containing 102 points is based on locations from a geological structure map (Clarke et al., 1989), locations visited during fieldwork, and interpretation of high resolution aerial photos from ArcGIS high resolution imagery (DigitalGlobe et al., 2021). The extent of these anomalies is variable, ranging from few meters to few hundred meters in diameter, however since the dataset consists of points, their extent cannot be considered in the analysis. Examples are shown in Fig. 4.

Power plant/well-head location layer. Since power plants and some well-heads have heat expressions as well, a GIS layer with their locations was created based on information provided by Kenya Electricity Generating Company PLC (KenGen) and photo interpretation. This dataset was not

included in the accuracy measures, but used for visual comparison of the results.

2.4. Data processing

The processing of the data consisted of pre-processing and anomaly detection, which will be described in the following sections.

The pre-processing of the data consists of georeferencing, georeferencing improvement, and masking of clouds and radiometric errors. Due to the fact that only nighttime imagery was used, no topographic correction was conducted.

Our georeferencing process uses the nearest neighbour resampling, and georeferencing information provided by the ECOSTRESS L1B GEO data but with two important adjustments: Firstly, data from one scan mirror side are used: The ECOSTRESS sensor is using a push-whisk scanning principle with a continuously rotating double-sided mirror. The detector array of 256 pixels scans the field of view with one side of the mirror; the next scan is using the other side. There are always a few pixels overlap between the two scans (Logan and Smyth, 2019). During the analysis, a 2-pixel geolocation offset between adjacent scans was discovered. As a result, the nearest neighbour algorithm, which by default is used in the standard georeferencing process, leaves a chessboard pattern (Logan, 2022), that could influence the anomaly detections. We therefore adapted the georeferencing algorithm to use pixels from only one scan in the overlapping areas. This approach creates a discontinuity line between the scans, however these lines do not influence the detection results.

Secondly, an improved georeferencing approach was used: The georeferencing included in the standard processing of ECOSTRESS images is based on an image matching algorithm (described in ECOSTRESS
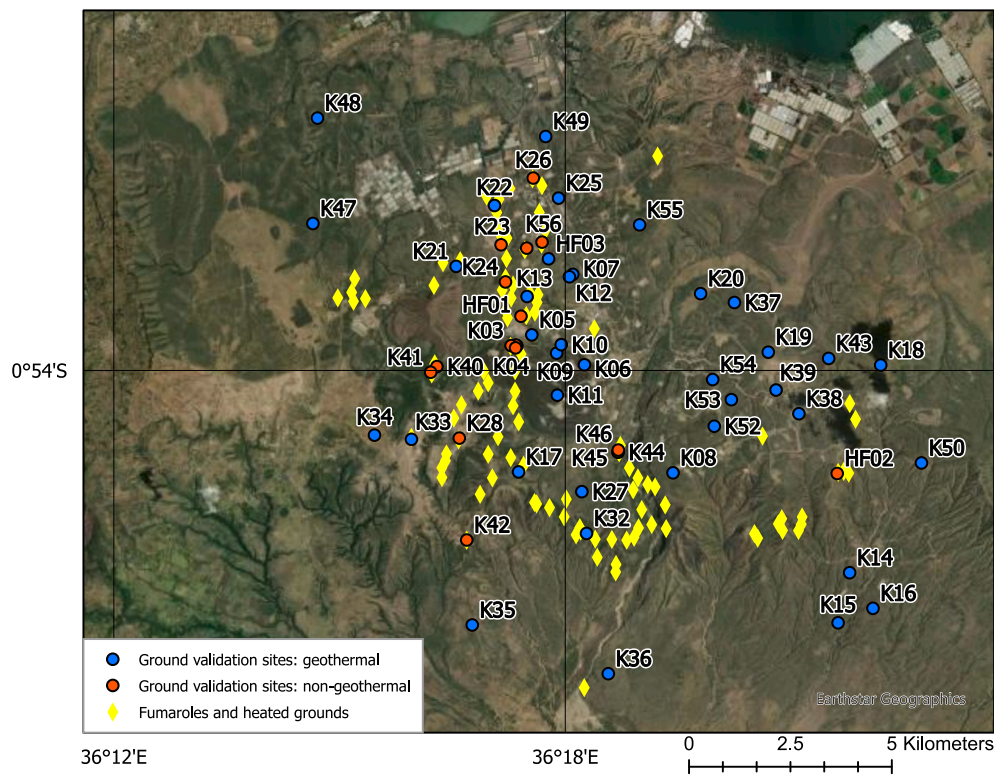
Fig. 3. Auxiliary data used for validation: ground validation sites from the field work (red and blue dots), and fumarole and heated ground locations (yellow diamonds). Background: high resolution imagery. (For interpretation of the references to colour in this figure legend, the reader is referred to the web version of this article.)
Source: ArcGIS Map Service: Esri, Maxar, Earthstar Geographics, and the GIS User Community.

Level-1 Product User Guide Logan and Smyth, 2019). In the imagery used, the accuracy of georeferencing was not accurate enough: a mean error of 14.9 pixel was observed; thus, it was necessary to improve it. The procedure used to improve the georeferencing of the imagery is based on matching of water body edges between the reference and target image. Due to dynamic land cover changes in the region, which include strong changes of water levels (and thus water body extent), a separate up-to-date reference is created for each target image. Further details on the method are described in Soszynska et al. (2023).

Some pixels have been excluded from further analysis, as they can contain cloud cover or their radiometric quality is insufficient, due to technical reasons (*e.g.*, radiometric artefacts). Such pixels can influence anomaly detection and cause errors in the resulting map. The low-accuracy and cloud pixels were masked using information provided in the Quality Control layer of the image product. Any pixel with quality flag "mandatory" greater than 0 (best quality: meaning no cloud detection, no missing data, and no indicators suggesting high water vapour), was masked. After this step, the data were ready for the detection algorithm.

A *detection product* for each image is calculated by finding outlying LST values in subsets of the image. The final results of the processing are the *anomaly index map*, and the *binary anomaly map*, which are created from a time series of detection products.

To derive a detection product, a kernel of 25×25 pixels is iterated over the image, and for each kernel position, its central pixel is analysed. To test whether the pixel is anomalous, its LST is compared to its direct neighbourhood (the kernel). A detection threshold is defined separately for each kernel position: detection threshold = $median_{\text{kernel}} + 2$ K. If the LST of the analysed pixel exceeds the detection threshold, it is considered anomalous. The $median_{\text{kernel}} + 2$ K detection threshold was chosen based on the modelling of ECOSTRESS LSTE accuracy provided in Hook and Hulley (2018), with the assumption that below this value, noise might influence the detection.

The kernel size of 25×25 pixels was chosen to be significantly larger than the known geothermal anomalies in the field. However, if the area of a geothermal anomaly comprises most of the considered kernel, the detection threshold would be calculated mostly from anomalous pixels, which leads to an omission error. In such a case, the median LST of the kernel will be substantially larger than the median LST of the image of the entire study area. Therefore, the median temperature of each considered kernel is tested first, and in case it exceeds the median of the image by more than 1 K, the kernel size is enlarged by 1 pixel in each direction. The enlargement is repeated until the median LST of the kernel is less than 1 K above image median (Fig. 5).

The method yields detections that contain possible geothermal anomalies, from a single image (called "detection product"). The detection products are subsequently summed and post-processing is conducted. The summed product is normalised to the range between 0–100 in values to enhance interpretation.

The changes of the geothermal activity of an area happen over many years, which makes it different from, *e.g.*, flooding or fire, image artefacts, and cloud-mask errors. To distinguish geothermal anomalies from short-term events, post-processing on the resulting anomaly index map is conducted to maintain long-term persisting detections only. All pixels that were detected in two images or less are masked. In addition, isolated pixel detections were removed in the final product, to ease interpretation. This product is further referred to as the "anomaly index map", and contains anomaly index values representing the percentage of images in which the pixel was detected as an anomaly.

To quantify the detection accuracy compared to ground data, a binary map of detections was created, by masking all the pixels which are detected in two or less images and setting the rest of the detected pixels to 1. The result is a map with detections and background ("binary anomaly map"), where each detected contiguous area was given a unique label.
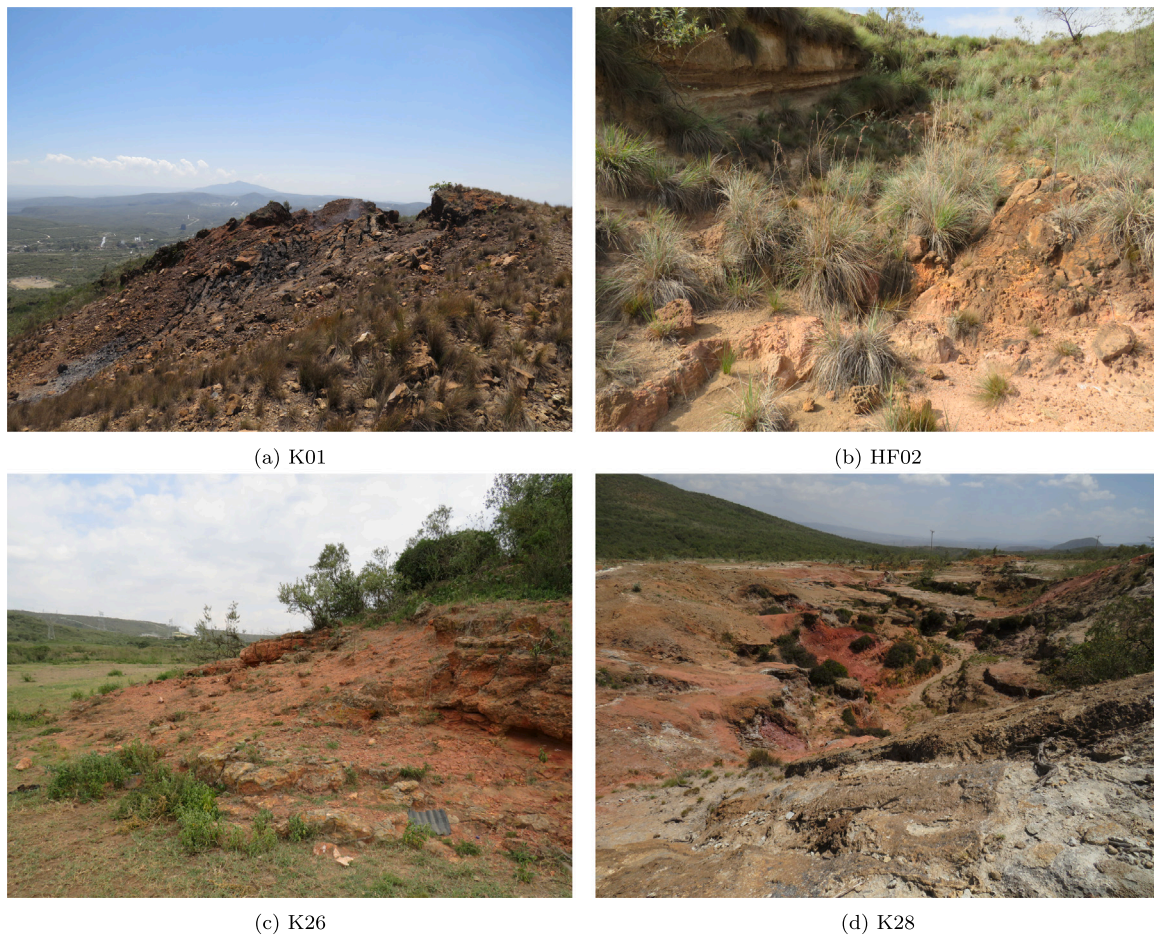
(a) K01

(b) HF02

(c) K26

(d) K28

Fig. 4. Field work documentation photos for example fumaroles.

2.5. Validation

The validation of the obtained results was done threefold. First, the anomaly index map was compared to the fumarole and heated ground location layer. This was done by correlating each pixel with an anomaly index value greater than 0 with the Euclidean distance to the nearest fumarole/heated ground. This procedure allows for the quantitative comparison of the spatial patterns of the geologic structure (depicted by the fumarole and heated ground locations dataset) to the anomaly map. Fumaroles and heated grounds do not have clear boundaries, and therefore it is difficult to account for their extent. The fumarole/heated ground location layer contains points only, and therefore using the Euclidean distance to the nearest fumarole/heated ground allows accounting for their extent. No spatial correlation between the two datasets yields random distribution of the scatter plot, while a high spatial correlation results in concentration of high anomaly index values in the shortest distances to the nearest fumarole or heated ground.

In the second validation approach, the binary anomaly map was treated as a classification result, and compared to the ground validation sites, which were divided into two categories: geothermal and non-geothermal. Thus, both commission and omission errors could be estimated, as well as producer's and user's accuracies (as described in Lillesand et al. 2015). Producer's accuracy in our case defines how many geothermal ground validation sites correctly detected in the binary anomaly map are found in relation to the number of all geothermal ground validation sites (i.e., number of true positives divided by all positive (geothermal) ground validation sites). Omission error complements the producer's accuracy and describes how many

geothermal ground validation sites have not been detected in relation to all geothermal ground validation sites. User's accuracy describes in our research the proportion of correctly detected geothermal ground validation sites to all ground validation sites detected as geothermal in the binary anomaly map (i.e., true positives divided by the sum of true and false positives). Commission error complements the user's accuracy, and describes how many ground validation sites falsely detected in the binary anomaly map are there in comparison to all ground validation sites detected as geothermal (i.e., number of false positives divided by the sum of true and false positives). To accommodate for a georeferencing error, a tolerance of ± 2 pixels was introduced when comparing the anomaly map to the ground validation locations. Hence, a true positive anomaly detection consists of a geothermal ground validation site, and one or several detected pixels within a 2-pixel radius in the binary anomaly map. A true negative result, on the other hand, consists of a non-geothermal ground validation site and not a single detected pixel within a 2-pixel radius in the binary anomaly map. All other situations represent either false positives or negatives in the error matrix. In addition, an auxiliary dataset containing fumarole and heated ground locations, was used to calculate the producer's accuracy. The addition of the 2-pixel radius in validation of the binary detection map creates a bias, by increasing the number of false positive detections. We discuss this bias and its consequences in Section 4.

To get a robust estimation on how reliable the results of the presented method are, we also compared the detection accuracies reported here, against what the detection accuracy would look like on a completely random classification. For this step, the same parameters are used as in the anomaly index map and binary anomaly map (study area range, pixel size) and create randomised anomaly maps. The
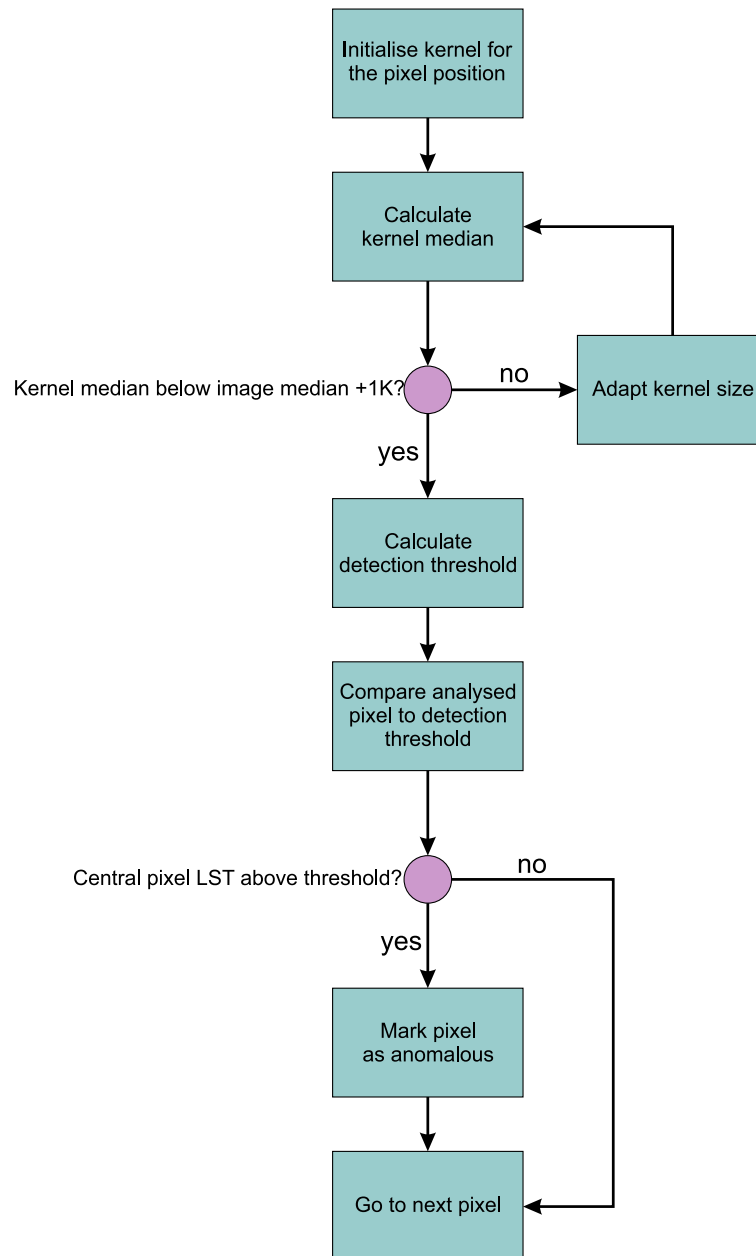
Fig. 5. Detection method of anomalous pixels in an image.

randomised anomaly maps were created by randomly distributing detections (acquired from the ECOSTRESS anomaly map) through the image area: in the first case in the form of contiguous areas, which were randomly rotated and randomly located in the study area (random binary anomaly map), in the second case the anomaly index value per pixel (random anomaly index value). Both randomisation attempts were conducted 100 times, and the accuracy results provided in Section 3 were calculated by averaging over all random combinations.

Lastly, the binary anomaly map was visually inspected, compared to the auxiliary datasets and to the visual inspection protocols from the ground validation sites, to find potential sources of errors.

3. Results

3.1. Anomaly maps

The anomaly index map has a distinct distribution, forming multiple clusters (Fig. 6). Approximately 25% of the detected pixels have the lowest anomaly index value (<10), while an anomaly index value above 50 is found in less than 5% of the pixels.

The binary map of detected geothermal anomalies, presented in Fig. 7, contains a total of 267 detected areas. The detected anomalies cover together 43 km^2, which is approximately 11% of the study area. The detection method identified two very large geothermal areas (which comprise approximately 18 and 4 km^2 respectively), 16 smaller, and multiple very small geothermal anomalies located mostly in the southern part of the study area.

3.2. Validation

A visual comparison shows some similarity between the known fumaroles or heated ground locations and the detected areas (Fig. 8(a)). For instance, fumaroles and heated grounds in the bottom-centre of the map (forming a U-shaped group) are clearly depicted in the detection map. At the same time, some distinct groups of fumaroles have not been detected at all (e.g., the group to the East from the U-shaped fumarole
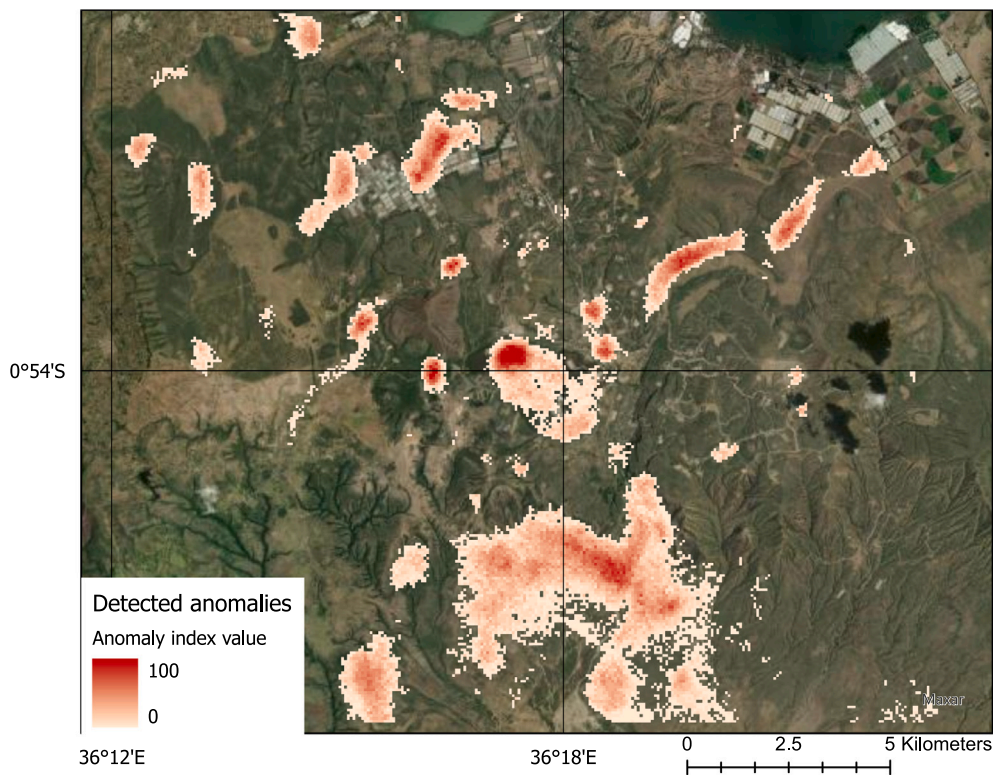
Fig. 6. Anomaly index map. The anomaly index values per pixel represent the percentage of images in which the pixel was detected as an anomaly.
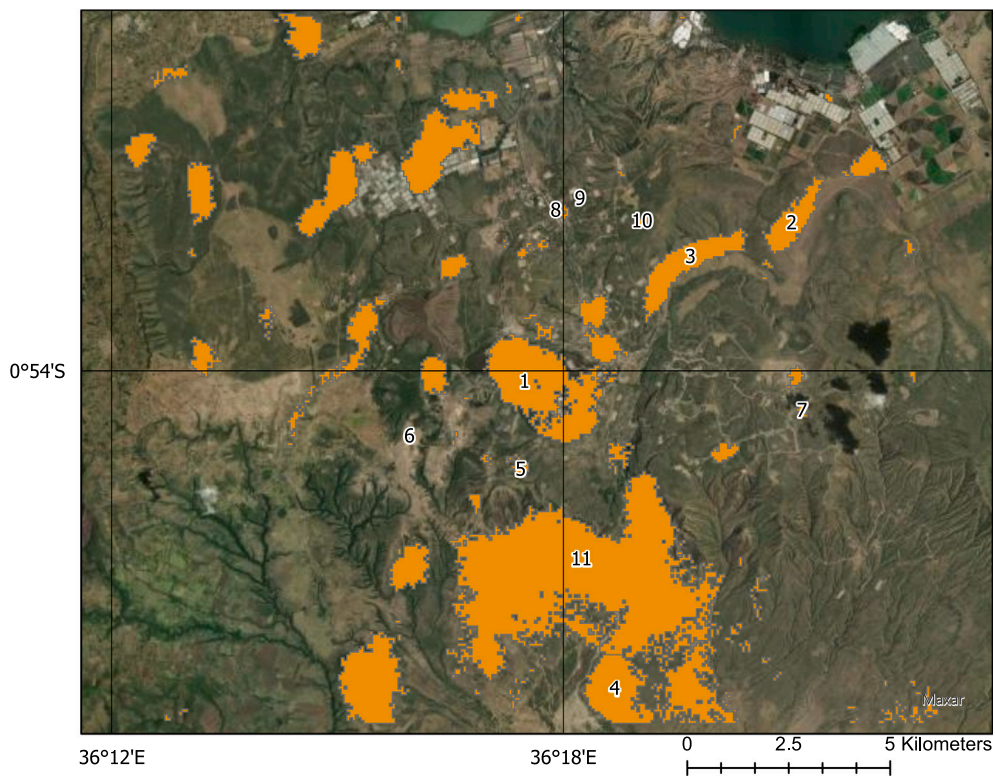
Fig. 7. The binary map of detected surface temperature anomalies. For clarity, only labels of the anomalies referenced further in text have been kept.

group). Additionally, some areas detected in the satellite data are not reflected in the fumarole/heated ground locations. This might happen due to an error, but it is also possible that new fumaroles or heated grounds are detected with the proposed method.

To give a more quantified result for the spatial pattern agreement, the anomaly index can be correlated to the distance to the nearest fumarole or heated ground, which accounts for remaining geolocation errors of the images, and the fact that fumaroles are represented as

(a) Anomaly index value and fumarole/heated ground locations. The fumaroles/heated ground locations are marked as blue "x". Zero values in the figure were removed for processing. The x- and y- axis are ECOSTRESS 70 m pixels, the imagery is North-up.
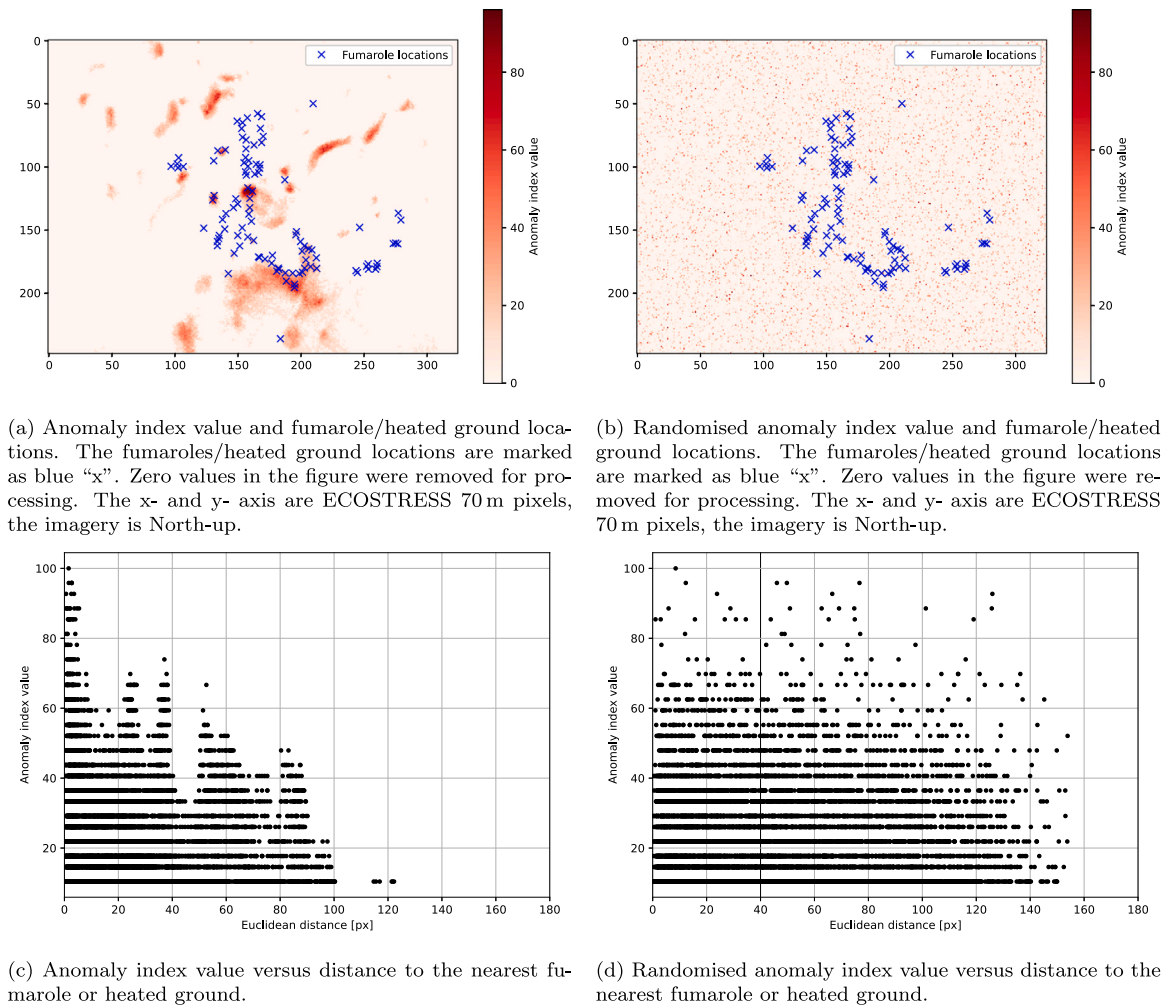

(b) Randomised anomaly index value and fumarole/heated ground locations. The fumaroles/heated ground locations are marked as blue "x". Zero values in the figure were removed for processing. The x- and y- axis are ECOSTRESS 70 m pixels, the imagery is North-up.

(c) Anomaly index value versus distance to the nearest fumarole or heated ground.

(d) Randomised anomaly index value versus distance to the nearest fumarole or heated ground.

Fig. 8. Anomaly index value in comparison to the distance to the nearest fumarole or heated ground. The area depicted in plots is the study area.

point in the reference data, and their area is neglected. The comparison presented in Fig. 8(c) has a skewed distribution with the highest peak at the lowest Euclidean distance, and multiple smaller peaks. The highest anomaly index values are found at the lowest distance to the nearest fumarole or heated ground, which suggests a correct sensitivity of the detection method. The secondary peaks suggest that some large detections are located in areas where no fumaroles or heated grounds are present (for example, in the north-western part of the study area).

A similar comparison was conducted for a randomised anomaly map (Fig. 8(b)). The pixels with high anomaly index values are spread randomly in the image, while fumaroles and heated grounds are concentrated in the centre of the map. In Fig. 8(d), the distribution of the ground validation sites is close to random, especially for the highest anomaly index.

Ground validation sites were used to calculate confusion matrices and accuracy measures of the binary anomaly map as well as randomised versions of the anomaly map (described in Section 2.5) in Tables 2, 3, 4 and 5. The confusion matrix for the detection method (Table 2) presents the highest number of correctly classified geothermal ground validation sites (geothermal in the reference and in detection), which is confirmed by the high producer's accuracy in Table 5.

Overall, producer's and user's accuracy, as well as commission and omission errors, are calculated from the ground validation sites. The producer's accuracy calculated from fumarole and heated ground location adds information to the measures from ground validation sites. Generally, the detection method obtained several percent points higher overall accuracy than its randomised versions. The producer's

Table 2

Confusion matrices for the detection method.

		Detection		Σ reference
		Geothermal	Non-geothermal	
Reference	Geothermal	14	3	17
	Non-geothermal	15	24	39
	Σ detection	29	27	56

Table 3

Confusion matrices for the randomised contiguous areas.

		Randomised contiguous areas		Σ reference
		Geothermal	Non-geothermal	
Reference	Geothermal	6 ± 3.7	11 ± 3.7	17
	Non-geothermal	13 ± 3.9	26 ± 3.9	39
	Σ Randomised contiguous areas	19 ± 3.8	37 ± 3.8	56

accuracy is much higher in the anomaly map, which means that the geothermal ground validation sites are found much more reliably in the anomaly map (48% points higher in randomised contiguous areas, and 63% in randomised pixels). The user's accuracy of the anomaly map is slightly lower than the producer's accuracy, which causes that the overall accuracy decreases as well. The high commission error in the binary detection map causes the overall accuracy to decrease,

Table 4
Confusion matrices for the randomised pixels.

		Randomised pixels		Σ reference
		Geothermal	Non-geothermal	
Reference	Geothermal	3 ± 1.6	14 ± 1.6	17
	Non-geothermal	8 ± 2.4	31 ± 2.4	39
	Σ Randomised pixels	11 ± 2.0	45 ± 2.0	56

Table 5
Accuracy results for the detection binary map and for the randomised versions using random contiguous areas and randomised anomaly index values. The results for randomised versions are averaged over 100 random maps. The accuracies have been calculated using ground validation sites (both geothermal and non-geothermal points), and fumarole locations.

	Detection	Randomised contiguous areas	Randomised pixels
Overall accuracy (geothermal and non-geothermal)	68%	57% ± 7.1%	60% ± 4.9%
Producers accuracy (geothermal)	82%	34% ± 22.0%	19% ± 9.5%
Producers accuracy (non-geothermal)	62%	68% ± 9.9%	78% ± 6.2%
Users accuracy (geothermal)	48%	29% ± 13.2%	28% ± 11.5%
Users accuracy (non-geothermal)	89%	71% ± 6.8%	69% ± 2.9%
Omission error (geothermal)	18%	66% ± 22.0%	81% ± 9.5%
Omission error (non-geothermal)	38%	32% ± 9.9%	22% ± 6.2%
Commission error (geothermal)	52%	71% ± 13.2%	72% ± 11.5%
Commission error (non-geothermal)	11%	29% ± 6.8%	31% ± 2.9%
Fumarole accuracy	55%	33% ± 13.0%	21% ± 4.4%

likely due to the introduction of the 2-pixel tolerance. Nevertheless, the user's accuracy is still higher in the anomaly map than in the randomised versions. Importantly, the omission error of the geothermal ground validation sites is much higher in the randomised versions of the anomaly map. The same situation is visible in the fumarole/heated ground accuracy (which is producer's accuracy for the fumarole and heated ground location layer): this accuracy measure in the anomaly map is higher than in the randomised versions. In general, the anomaly map clearly identifies geothermal areas more accurately, although the overall accuracy is not significantly higher. At the same time, the accuracies for the non-geothermal ground validation sites are similar in all versions of the map, which is explained by the fact that the non-geothermal ground validation sites comprise a majority of the ground validation dataset (70% of all ground validation sites) as well as the majority of the pixels (89% of all pixels). Thus, the statistical probability that a pixel considered non-geothermal will also cover a point which is non-geothermal in reality is 62%. This introduces an additional positive accuracy bias for the randomised versions of the map.

A visual inspection of the binary anomaly map allows identifying several omitted geothermal ground validation sites, and presume the cause of omission (Fig. 9). For instance, the ground validation sites K26 and HF02 were omitted most probably due to too small size of the geothermal area (which is approximately 40% of a pixel area in both cases), and vegetation coverage causing insulation. Another possibility for explaining the omission of HF02 is the low temperature of the anomaly (approximately 323 K at 20 cm depth). This is an area with relict fumarolic activity which is in some distance to the sites with strong heat signatures. Another reason for omission error, can be presumed at the site K24. This site is placed within a terrain crack covered by vegetation, possibly causing masking of the thermal signal and directing the majority of thermal emission not towards the sensor.

Several sources of commission errors can also be interpreted on the map. In the case of ground validation sites K25, K38, and K55, the detections are false positive due to a thermal signal from a neighbouring power plant or well-head (detections 8 and 9 in Fig. 7). Altogether, 11 out of 16 power plant or well-heads have prominent thermal signatures which are detected in the binary anomaly map. Although these areas do

not fulfil the temperature conditions to be considered geothermal (see Section 2 for details), they do emit thermal radiation higher than their surroundings, and therefore are detected as anomalies. Heat signature from the neighbouring active fumaroles can be another cause for a commission error, due to signal being spread among the neighbouring pixels. This is the case of ground validation sites K17, K32, and K33. In the anomaly map, detections are validated within a tolerance limit of ±2 pixels, which causes false positive detection in these ground validation sites (detections 5, 6 and 11). Lastly, ground validation sites K11 and K36 are placed on rocky hills with barely any vegetation, which possibly lose heat in the night more slowly than their surroundings, due to a high heat capacity (detections 1 and 4).

4. Discussion

Finding new, renewable and sustainable sources for energy production, such as heat from volcanic geothermal systems, is an important task to support energy transition from fossil fuels. The particular orbit of the International Space Station (on which the ECOSTRESS sensor is mounted), allows acquiring imagery at different times, which is a promising asset for early exploration of geothermal sources. ECOSTRESS data have not been used for automated geothermal anomaly detection until now, and testing its detection ability is an important task.

The main difficulty in detecting the geothermal anomalies is the fact that they are usually rather small and weak thermal emission sources, especially with respect to water bodies and cities in an image. Therefore, a kernel based method was developed that uses statistical measures of the observed image subset for derivation of anomalous pixels. Since our method allows considering the direct surroundings of an anomaly, even a weak geothermal anomaly can be identified because of its contrast to its neighbourhood, given that the neighbourhood does not contain warmer surfaces, such as water bodies or urbanised areas. A kernel-size adaption was added in our method, to account for large anomalies that would be omitted in a smaller kernel.

Using a time series of nighttime ECOSTRESS data, allowed to detect 82% of geothermal anomalies in our study area. Since remote sensing detection of geothermal anomalies serves as a preliminary exploration support, it is much more important to obtain high producer's accuracy than high user's accuracy. This strategy accepts a bias towards detection, because false positives potentially provide less financial losses than false negatives. This is fulfilled in the presented results: the producer's accuracy achieved in the anomaly map is high (although the user's accuracy is lower). The validation procedure introduces a bias, because a non-geothermal point will be considered a false negative, when a detection was made within 2 pixel distance.

In order to better understand the accuracy results, it is important to find the potential error sources in the anomaly map. The visual inspection of the anomaly map, allowed identifying five potential sources of errors related to the terrain: (1) Terrain features, vegetation, and steam, which can cover the anomaly or block the thermal emission in the sensor's direction, (2) heat capacity and heat decay of surfaces, which can cause false positive detection, (3) too low temperature of the anomaly to be detected, (4) too small extent of the anomaly to be detected, and (5) uncertainty of what a true detection is. The last point refers to the fact, that we do not have a clear understanding of the anomaly characteristics necessary to allow a detection in a space-borne thermal image. The method is not designed to detect fumaroles or heated grounds, but rather surface temperature anomalies, such as geothermal grounds, although in some cases it detects fumaroles and heated grounds very accurately. In fact, detection 6 (Fig. 7) is at a fumarole location marked in the fumarole/heated ground locations, while at the same time the measurement at the ground validation site K33 revealed it as non-geothermal (Fig. 9).

The land cover might induce errors; for instance, in areas where vegetation cover is not present, heating up during the day will be
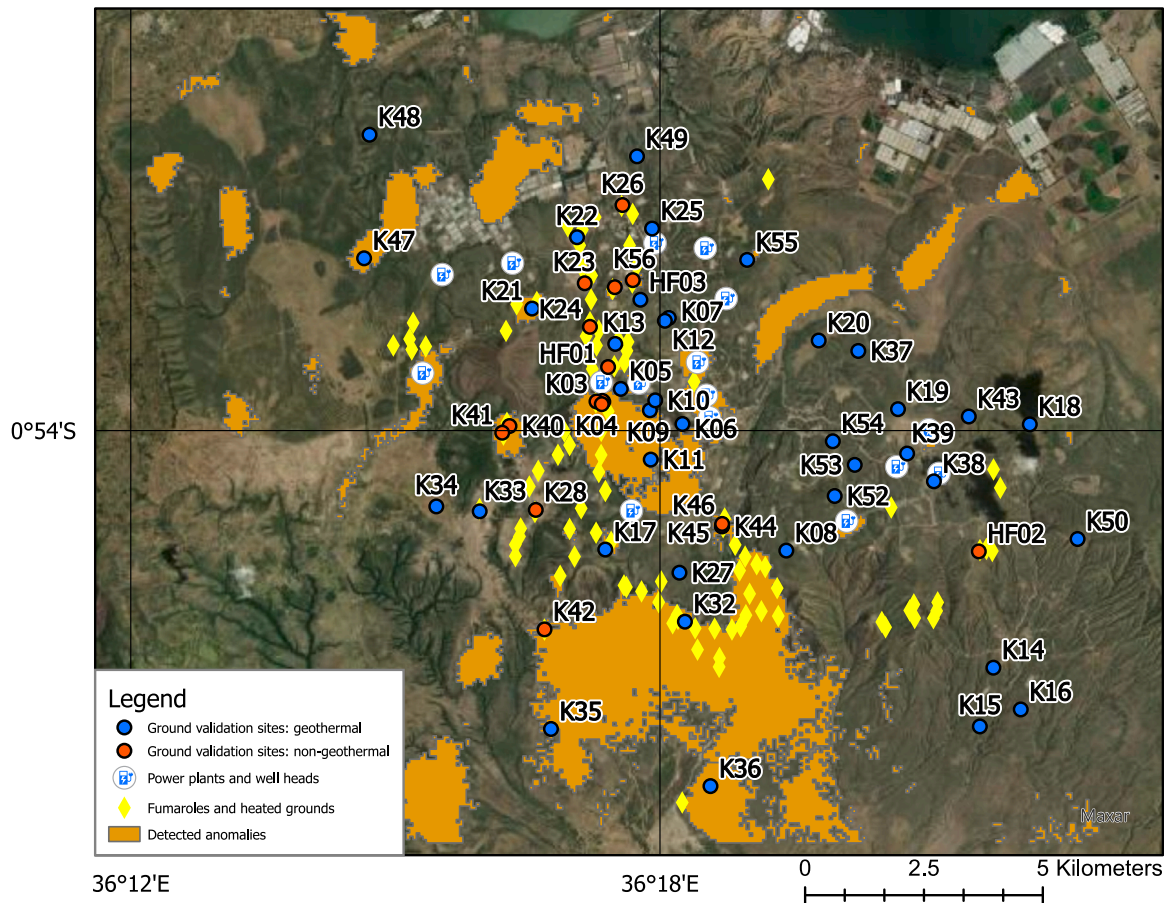
Fig. 9. Binary anomaly map and auxiliary layers: ground validation sites (labelled), fumarole and hot ground locations, and power plant/well-head locations.

stronger. It was observed that the LST of bare grounds is higher than the LST of vegetated areas all throughout the night. Hence, non-vegetated areas will appear warmer in the imagery, and possibly cause a false detection. A detailed study on vegetation (or in broader terms: land cover) would be beneficial for understanding of remote sensing potential for geothermal anomaly detection.

Some errors might be introduced, due to the form of the terrain. This conclusion is also found in Coolbaugh et al. (2007) and Gutiérrez et al. (2012). In our case, detections 2 and 3 in Fig. 7 are located at the steep edges of a gorge. The gorge appears cooler in the ECOSTRESS imagery, possibly because it receives less insolation. Contrast to a neighbouring cooler area may cause a commission error, however it was not possible to verify these detections during the field work, due to its limited accessibility.

Another source of commission errors related to the terrain is slope aspect (Eneva et al., 2006). Although for the equatorial regions like Olkaria, aspect may not play the most important role (especially for the equinox periods), for other regions located further away from the Equator, heating up of southern or northern slopes can be much stronger than others. This heat may still be visible in nighttime imagery, notably if the image acquisition time is shortly after sunset.

Some fumaroles and heated grounds in the study area release steam in irregular time intervals, which can obstruct the thermal emission from reaching the sensor. The steam occurrence is unpredictable and therefore its influence on detection accuracy is difficult to quantify. Since the fumaroles are monitored only from time to time (and never in the nighttime), there is no information on steam occurrence during the acquisition times of ECOSTRESS images.

All the previously described effects are additionally influenced by heat capacity, density, conductivity, and thermal emissivity of materials in a pixel. Different lithologies affect the situation: rock outcrops,

soil, and ash deposits will all have different cooling rates, in addition to different emissivity (Coolbaugh et al., 2007). Moreover, moisture will affect emissivity, and in some cases heat capacity (*e.g.*, of soil) as well (Coolbaugh et al., 2007). These effects play a considerable role in the accuracy of geothermal anomaly detection with remote sensing techniques. A detailed study regarding heat decay in different lithologies, weather conditions, and land cover types would be beneficial for the understanding of all those aforementioned effects.

Another group of error sources can be related to data and pre-processing. We observed that inaccurate cloud masking can lead to false positive detections; as clouds are colder than the land masses, the areas surrounding the clouds, will be detected as anomalies. Such detections were removed, if all pixels marked as anomalous in less than three images are removed in post-processing. Additionally, the georeferencing accuracy can introduce errors as well. The ±2 pixel buffer was included to account for such errors, although this introduces a positive bias towards detections and causes commission errors in some cases.

The sensitivity of a sensor, and image quality, play an important role for detection accuracy. The coarser the spatial resolution, the lower the contrast between the pixel containing the geothermal anomaly and surroundings, which is the most important parameter in for detection. Sharpness of images and low level of noise can additionally decrease this contrast. Generally, long-wave infrared Mercury–Cadmium–Telluride sensors are more prone to noise, than, for instance, mid-wave-IR sensors of the same type; in many cases, some line artefacts are visible in the image (e.g., visible in the north-eastern part of the ECOSTRESS image in Fig. 2). This leads to errors if line artefacts are not masked, but even in cases when line artefacts are correctly masked (*e.g.*, using quality flags provided with ECOSTRESS LST image)

an anomaly falling in such a line will be omitted. A sensitivity analysis of image quality, including the minimum size of the anomaly to be detected for the given ground sampling distance of a sensor, radiometric accuracy, Signal-to-Noise-Ratio, and Point-Spread-Function, would complement the analysis on feasibility of a sensor for this application.

The study area of Olkaria, Kenya, provides a typical example of geothermally active areas in the East African Rift. The study was limited to only one area, due to availability of reference data. The LST in Olkaria is fairly homogeneous, and the detection threshold of $median + 2\,K$ yields satisfactory results. The findings of this study are applicable to areas of similar characteristics, such as in other areas of the East African Rift, but possibly parameter values (*e.g.,* detection threshold) may require adjustments for other study areas. Factors such as snow cover, and climate differences possibly need to be accounted for in other study areas. It would be beneficial to test this approach in a different study area, possibly with different climate, to find out how regional characteristics influence the accuracy of detections.

Moreover, considering the accuracy of the results obtained, it is important to understand the limitations of the validation. The thermal anomalies presented in Fig. 7 were validated, by comparing the location of detections with reference layers: fumaroles and heated grounds, ground validation sites, and power plant/well-head locations. In the course of field work, it was not possible to visit all the places detected, and distribution of the ground validation sites was influenced by accessibility of the terrain. The accuracy results are possibly positively biased, because of the ± 2 pixel tolerance for detections. However, it is important to note that lack of ground validation site suggesting geothermal activity in specific detected areas, does not necessarily mean that these detections are false positive. At the same time, the geothermal ground validation sites are underrepresented: there are 17 geothermal ground validation sites, and 39 non-geothermal validation sites. This increases the probability that a non-geothermal ground validation site will be randomly associated to a non-detected pixel. Thus, the accuracy measures regarding the non-geothermal points are less reliable in the case of randomised anomaly maps.

In validation of detection results, a layer containing fumarole and heated grounds locations was used as a reference. Correlation of anomaly index values with distance to the nearest fumarole/heated ground provides an approximation of accuracy, however the interpretation requires some caution. Hydrothermal features, such as fumaroles, depend on geologic structures transporting hot water to the surface. The location and orientation of such structures depends on the geologic setting, and they may be located towards the edges of a larger surface temperature anomaly. Thus, a bias may occur in the validation. Additionally, fumaroles and heated grounds are very diverse in terms of size, activity, shape, sometimes even structure, and vegetation cover, which complicates detection significantly. In order to assess the accuracy of fumarole (and heated ground) detections, a deeper understanding of their features such as size, horizontal and vertical temperature gradients, and diurnal temperature cycle is needed, in addition to contextual information on features mentioned above.

5. Conclusions

In the presented study, we tested the feasibility of using ECOSTRESS data for automated detection of geothermal anomalies. The spatial resolution of ECOSTRESS is the highest available among thermal sensors as of 2023, and this is a big advantage for remote sensing of geothermal anomalies. Using ECOSTRESS data for preliminary exploration of geothermal anomalies is cost-effective, since the data is free to download. ECOSTRESS fulfils most of the requirements necessary for geothermal anomaly detection (nearer described in Section 1), however the high noise level, striping, and checkerboard pattern which occur in some parts of the image require special pre-processing, such as using an adjusted georeferencing method. This is the first study to test the potential of ECOSTRESS for automated solutions that can lead to development of global mapping of geothermal anomalies. Since other research publications rather acknowledged visibility of known anomalies, or compared temperatures, it is difficult to compare such results. We used kernel-based thresholding to automatically detect LST anomalies in Olkaria, Kenya, and analyse the results in a transparent, quantitative way. This allows to compare the accuracy with other methods or other data sources, such as ASTER or TIRS.

Geothermal anomalies can be identified with our approach in ECOSTRESS imagery with a producer's accuracy of 82%, which is on average 56% points better than in randomised anomaly maps. These results suggest that a time series ECOSTRESS data can be used for detecting geothermal anomalies, however more work needs to be conducted to better understands the shortcomings in the accuracy. Using time series decreases the influence of radiometric errors, clouds, and single-occurrence events, and the larger the time series, the more robust the resulting anomaly map. The method proposed is suitable for global application, especially since it accounts for various sizes of the anomalies.

Errors in the anomaly map can appear due to anomalies of insufficient dimensions, anomalies of low contrast to backgrounds, terrain features, and thermal inertia differences between surfaces. Image quality and accuracy of georeferencing also strongly contributes to the detection accuracy. Despite pre-processing, the image quality of ECOSTRESS may be one of the most important reasons for the low overall accuracy. Including georeferencing correction in the processing chain is a necessary step towards global mapping of geothermal anomalies with ECOSTRESS data.

From the analysis of the results, a number of new research questions can be found that can be grouped into the following future directions. The first direction is related to the image-quality limitations of ECOSTRESS space-borne imagery for the purpose of automated detection of geothermal anomalies. Additionally, a thorough characterisation of variables influencing detection accuracy is needed. Variables, such as terrain properties, and weather conditions, time of image acquisition, as well as thermal inertia of surfaces and sub-surface can potentially lead to large errors in detection maps, and understanding of these effects is crucial for further applications in this field. Research on these aspects would enhance understanding of remote sensing of geothermal anomalies, and thus potentially enable creation of globally applicable tools.

CRediT authorship contribution statement

Agnieszka Soszynska: Writing – original draft, Visualization, Validation, Methodology, Formal analysis, Data curation, Conceptualization. **Thomas Groen:** Writing – review & editing, Supervision, Methodology, Conceptualization. **Eunice Bonyo:** Writing – review & editing, Data curation, Conceptualization. **Harald van der Werff:** Writing – review & editing, Methodology, Conceptualization. **Robert Hewson:** Writing – review & editing, Conceptualization. **Robert Reeves:** Writing – review & editing, Conceptualization. **Christoph Hecker:** Writing – review & editing, Supervision, Resources, Project administration, Methodology, Conceptualization.

Declaration of competing interest

The authors declare that they have no known competing financial interests or personal relationships that could have appeared to influence the work reported in this paper.

Data availability

Reference data included, the code will be shared in GitHub marchewaka https://github.com/marchewaka/Geothermal_anomaly_detection.

Appendix A. List of used datasets

See Table A.6.

Table A.6
List of datasets used in the processing.

	Dataset name including the acquisition date and time in format YYYYMMDDTHHMMSS
1	ECOSTRESS_L2_LSTE_21021_016_20220322T005432_0601_01
2	ECOSTRESS_L2_LSTE_20899_011_20220314T040423_0601_01
3	ECOSTRESS_L2_LSTE_20784_022_20220306T184938_0601_01
4	ECOSTRESS_L2_LSTE_19716_033_20211227T215613_0601_01
5	ECOSTRESS_L2_LSTE_19404_017_20211207T180801_0601_01
6	ECOSTRESS_L2_LSTE_19099_015_20211118T014738_0601_01
7	ECOSTRESS_L2_LSTE_18602_028_20211017T022738_0601_01
8	ECOSTRESS_L2_LSTE_18228_017_20210923T000600_0601_01
9	ECOSTRESS_L2_LSTE_17670_030_20210818T020947_0601_01
10	ECOSTRESS_L2_LSTE_17294_018_20210724T234916_0601_01
11	ECOSTRESS_L2_LSTE_17172_016_20210717T025340_0601_01
12	ECOSTRESS_L2_LSTE_15383_015_20210324T002716_0601_01
13	ECOSTRESS_L2_LSTE_14650_016_20210204T190212_0601_01
14	ECOSTRESS_L2_LSTE_12759_016_20201005T192641_0601_01
15	ECOSTRESS_L2_LSTE_12698_016_20201001T205854_0601_01
16	ECOSTRESS_L2_LSTE_12576_007_20200924T000312_0601_01
17	ECOSTRESS_L2_LSTE_12217_021_20200831T205833_0601_01
18	ECOSTRESS_L2_LSTE_12156_025_20200827T223216_0601_01
19	ECOSTRESS_L2_LSTE_10578_018_20200518T025952_0601_01
20	ECOSTRESS_L2_LSTE_08572_020_20200109T180437_0601_01
21	ECOSTRESS_L2_LSTE_07336_021_20191022T013248_0601_02
22	ECOSTRESS_L2_LSTE_06108_017_20190803T210453_0601_02

Appendix B. Supplementary data

Supplementary material related to this article can be found online at https://doi.org/10.1016/j.rse.2024.114103.

References

Abubakar, A.J., Hashim, M., Pour, A.B., 2019. Remote sensing satellite imagery for prospecting geothermal systems in an aseismic geologic setting: Yankari park, Nigeria. Int. J. Appl. Earth Obs. Geoinf. 80, 157–172. http://dx.doi.org/10.1016/j.jag.2019.04.005.

Calvin, W.M., Coolbaugh, M., Kratt, C., Vaughan, R.G., Calvin, W., 2005. Application of remote sensing technology to geothermal exploration. In: Geological Society of Nevada Symposium: Window to the World, Reno, Nevada. pp. 1083–1089.

Chan, H.-P., Chang, C.-P., 2018. Exploring and monitoring geothermal and volcanic activity using satellite thermal infrared data in TVG, Taiwan. Terr. Atmos. Ocean. Sci. 29 (4), http://dx.doi.org/10.3319/TAO.2018.01.22.01.

Chan, H.-P., Chang, C.-P., Dao, P.D., 2018. Geothermal anomaly mapping using landsat ETM+ data in ilan plain, northeastern Taiwan. Pure Appl. Geophys. 175 (1), 303–323. http://dx.doi.org/10.1007/s00024-017-1690-z.

Clarke, M., Woodhall, D., Mwangongo, F., Korio, R., Ndogo, M., Ledgard, M., Kinyariro, J., 1989. Geothermal activity and structure of longonot volcano, the greater olkaria and eburru volcaninc complexes, and adjacent areas.

Coolbaugh, M., Kratt, C., Fallacaro, A., Calvin, W., Taranik, J., 2007. Detection of geothermal anomalies using advanced spaceborne thermal emission and reflection radiometer (ASTER) thermal infrared images at bradys hot springs, nevada, USA. Remote Sens. Environ. 106 (3), 350–359. http://dx.doi.org/10.1016/j.rse.2006.09.001.

Dickson, M.H., Fanelli, M., 2013. Geothermal Energy: Utilization and Technology. Routledge, London, http://dx.doi.org/10.4324/9781315065786.

DigitalGlobe, GeoEye, i-cubed, USDA FSA, USGS, AEX, Getmapping, Aerogrid, IGN, IGP, swisstopo, GIS User Community, 2021. World Imagery.

DiPippo, R., 2012. Butterworth-Heinemann, Oxford, http://dx.doi.org/10.1016/C2014-0-02885-7.

Eneva, M., Coolbaugh, M., Combs, J., 2006. Application of satellite thermal infrared imagery to geothermal exploration in east central california. GRC Trans. 30, 407–412, https://www.academia.edu/download/36342854/Eneva_et_al_GRCvol30_2006.pdf.

Gemitzi, A., Dalampakis, P., Falalakis, G., 2021. Detecting geothermal anomalies using landsat 8 thermal infrared remotely sensed data. Int. J. Appl. Earth Obs. Geoinf. 96, 102283. http://dx.doi.org/10.1016/j.jag.2020.102283.

Gutiérrez, F.J., Lemus, M., Parada, M.A., Benavente, O.M., Aguilera, F.A., 2012. Contribution of ground surface altitude difference to thermal anomaly detection using satellite images: Application to volcanic/geothermal complexes in the andes of central Chile. J. Volcanol. Geotherm. Res. 237, 69–80. http://dx.doi.org/10.1016/j.jvolgeores.2012.05.016.

Hecker, C., Kuenzer, C., Zhang, J., 2007. Remote-sensing–based coal-fire detection with low-resolution MODIS data, geology of coal fires: case studies from around the world: geological society of America. Rev. Eng. Geol. 18, 229–239. http://dx.doi.org/10.1130/2007.4118(15).

Hewson, R., Mshiu, E., Hecker, C., van der Werff, H., van Ruitenbeek, F., Alkema, D., van der Meer, F., 2020. The application of day and night time ASTER satellite imagery for geothermal and mineral mapping in east africa. Int. J. Appl. Earth Obs. Geoinf. 85, 101991.

Hook, S., 2023. ECOSTRESS, SBG and HYTES Status and Results. NASA, Accessed on 07 September 2023.

Hook, S.J., Hulley, G.C., 2018. ECOSTRESS level-2 land surface temperature and emissivity algorithm theoretical basis document. https://ecostress.jpl.nasa.gov/downloads/atbd/ECOSTRESS_L2_ATBD_LSTE_2018-03-08.pdf. Accessed on 07 September 2023.

Kuenzer, C., Zhang, J., Li, J., Voigt, S., Mehl, H., Wagner, W., 2007. Detecting unknown coal fires: synergy of automated coal fire risk area delineation and improved thermal anomaly extraction. Int. J. Remote Sens. 28 (20), 4561–4585. http://dx.doi.org/10.1080/01431160701250432.

Lee, K.C., 2004. Geothermal power generation. In: Cleveland, C.J. (Ed.), Encyclopedia of Energy. Elsevier, New York, pp. 875–893. http://dx.doi.org/10.1016/B0-12-176480-X/00347-8, https://www.sciencedirect.com/science/article/pii/B012176480X003478.

Lillesand, T., Kiefer, R.W., Chipman, J., 2015. Remote Sensing and Image Interpretation. John Wiley & Sons.

Logan, T., 2022. L1 Calibration and Geolocation. NASA JPL, Accessed on 7 September 2023.

Logan, T., Smyth, M., 2019. ECOsystem spaceborne thermal radiometer experiment on space station (ECOSTRESS) mission level 1 product user guide.

Mock, J.E., Tester, J.W., Wright, P.M., 1997. Geothermal energy from the earth: its potential impact as an environmentally sustainable resource. Annu. Rev. Environ. Resour. 22, 305. http://dx.doi.org/10.1146/annurev.energy.22.1.305.

Munyiri, S.K., 2016. Structural Mapping of Olkaria Domes Geothermal Field Using Geochemical Soil Gas Surveys, Remote Sensing and GIS (Ph.D. thesis).

Omenda, P.A., 1998. The geology and structural controls of the olkaria geothermal system, Kenya. Geothermics 27 (1), 55–74. http://dx.doi.org/10.1016/S0375-6505(97)00028-X.

Prayogo, A., Maryanto, S., Nadhir, A., 2019. Spatio-temporal change of land surface temperature at tiris Geothermal Potential Area, east java, Indonesia. Pak. J. Geol. 3 (1), 13–21. http://dx.doi.org/10.2478/pjg-2019-0002.

Qin, Q., Zhang, N., Nan, P., Chai, L., 2011. Geothermal area detection using landsat ETM+ thermal infrared data and its mechanistic analysis — A case study in tengchong, China. Int. J. Appl. Earth Obs. Geoinf. 13 (4), 552–559. http://dx.doi.org/10.1016/j.jag.2011.02.005.

Romaguera, M., Vaughan, R.G., Ettema, J., Izquierdo-Verdiguier, E., Hecker, C., Van der Meer, F., 2018. Detecting geothermal anomalies and evaluating LST geothermal component by combining thermal remote sensing time series and land surface model data. Remote Sens. Environ. 204, 534–552. http://dx.doi.org/10.1016/j.rse.2017.10.003.

Scott, B., 2012. Guideline for Mapping and Monitoring Geothermal Features. Bay of Plenty Regional Council.

Silvestri, M., Buongiorno, M.F., Romaniello, V., Marotta, E., Caputo, T., Sessa, E.B., Belviso, P., Avvisati, G., Musacchio, M., Teggi, S., 2020a. Multiscale and multisensor observations on geothermal area: 2019 acquisitions over parco delle biancane and sasso pisano (Italy). In: IGARSS 2020-2020 IEEE International Geoscience and Remote Sensing Symposium. IEEE, pp. 6002–6005. http://dx.doi.org/10.1109/IGARSS39084.2020.9323993.

Silvestri, M., Romaniello, V., Hook, S., Musacchio, M., Teggi, S., Buongiorno, M.F., 2020b. First comparisons of surface temperature estimations between ECOSTRESS, ASTER and landsat 8 over Italian volcanic and geothermal areas. Remote Sens. 12 (1), 184. http://dx.doi.org/10.3390/rs12010184.

Soszynska, A., van der Werff, H., Hieronymus, J., Hecker, C., 2023. A new and automated method for improving georeferencing in nighttime thermal ECOSTRESS imagery. Sensors 23 (11), 5079.

van der Meer, F., Hecker, C., van Ruitenbeek, F., van der Werff, H., de Wijkerslooth, C., Wechsler, C., 2014. Geologic remote sensing for geothermal exploration: A review. Int. J. Appl. Earth Obs. Geoinf. 33, 255–269. http://dx.doi.org/10.1016/j.jag.2014.05.007.

Vaughan, R.G., Keszthelyi, L.P., Davies, A.G., Schneider, D.J., Jaworowski, C., Heasler, H., 2010. Exploring the limits of identifying sub-pixel thermal features using ASTER TIR data. J. Volcanol. Geotherm. Res. 189 (3–4), 225–237. http://dx.doi.org/10.1016/j.jvolgeores.2009.11.010.

Vaughan, R.G., Keszthelyi, L.P., Lowenstern, J.B., Jaworowski, C., Heasler, H., 2012. Use of ASTER and MODIS thermal infrared data to quantify heat flow and hydrothermal change at yellowstone national park. J. Volcanol. Geotherm. Res. 233, 72–89. http://dx.doi.org/10.1016/j.jvolgeores.2012.04.022.

Wang, K., Jiang, Q.-g., Yu, D.-h., Yang, Q.-l., Wang, L., Han, T.-c., Xu, X.-y., 2019. Detecting daytime and nighttime land surface temperature anomalies using thermal infrared remote sensing in dandong geothermal prospect. Int. J. Appl. Earth Obs. Geoinf. 80, 196–205. http://dx.doi.org/10.1016/j.jag.2019.03.016.

Watson, F.G., Lockwood, R.E., Newman, W.B., Anderson, T.N., Garrott, R.A., 2008. Development and comparison of landsat radiometric and snowpack model inversion techniques for estimating geothermal heat flux. Remote Sens. Environ. 112 (2), 471–481. http://dx.doi.org/10.1016/j.rse.2007.05.010.

Yuhendra, J.T.S.S., 2020. Assessment of landsat 8 TIRS data capability for the preliminary study of geothermal energy resources in west sumatra. Change 10, 11. http://dx.doi.org/10.12928/telkomnika.v18i5.16172.

Zhang, J., 2004. Spatial and Statistical Analysis of Thermal Satellite Imagery for Extraction of Coal Fire Related Anomalies (Ph.D. thesis). Vienna University of Technology.